Volume 1 | Number 1 | Jan 2013 | Pages 1–100

Catalysis Science & Technology

www.rsc.org/catalysis

ROYAL SOCIETY OF CHEMISTRY

ROYAL SOCIETY OF CHEMISTRY

www.rsc.org/catalysis

Magnetically recoverable catalysts containing Ru/RuO$_2$ and iron oxide nanoparticles show remarkable activity and selectivity in nitrobenzene-to-aniline hydrogenation

Catalysis Science & Technology

ARTICLE

Design of Ruthenium/Iron Oxide Nanoparticle Mixtures for Hydrogenation of Nitrobenzene to Aniline: Catalytic Behaviour Influenced by Iron Oxide Nanoparticles

R. Easterday[a], O. Sanchez-Felix[a], Y. Losovyj[a], M. Pink[a], B. D. Stein[b], D. G. Morgan[a], M. Rakitin[c], V. Yu. Doluda[c], M. G. Sulman[c], W. E. Mahmoud[d], A. A. Al-Ghamdi[d], Lyudmila M. Bronstein[a, d]*,

Here we report novel catalysts for nitrobenzene hydrogenation based on Ru/RuO$_2$ nanoparticles (NPs) and including iron oxide NPs, allowing magnetic recovery. The solvent type, reaction temperature, and the size and composition of initial iron oxide NPs are demonstrated to be the control factors determining synthesis outcomes including the degree of NP aggregation and catalytic properties. A complete characterization of the catalysts using transmission electron microscopy (TEM), X-ray powder diffraction (XRD), x-ray photoelectron spectroscopy (XPS), and energy dispersive x-ray spectroscopy (EDS) allowed assessment of the structure-property relationships. It is revealed that coexistence of the Ru/RuO$_2$ and iron oxide NPs in the catalyst as well as the proximity of two different NP types lead to significantly higher aniline yields and reaction rates. The catalytic properties are also influenced by the type of iron oxide NPs present in the catalytic samples.

Introduction

Recently, magnetically recoverable catalysts received considerable attention due to facile catalyst recovery.[1-6] Such catalysts allow eco-friendly processes and significant energy savings resulting in cheaper target products.[7-13] Catalysts containing Ru(0), ruthenium oxide or hydroxide on iron oxide supports were tested in oxidation, hydrogenation, and conversion of valuable substances,[14-20] accompanied, in some instances, by magnetic catalyst recovery.[19]

In this paper we report a novel method for development of magnetically recoverable ruthenium-based catalysts by formation of ruthenium nanoparticles (NPs) in the presence of well-defined iron oxide NPs. In our preceding work, we demonstrated fabrication of PtFe NPs by thermal decomposition of Pt acetylacetonate, Pt(acac)$_2$, in the presence of maghemite NPs.[21] The mixture of PtFe and iron oxide NPs showed a higher catalytic activity than that of purely PtFe NPs.[21]

Here, Ru(acac)$_3$ is used as a Ru source and iron oxide NPs of different compositions as an iron source. Depending on the

reaction conditions this may result either in a mixture of Ru/RuO$_2$ and iron oxide NPs or in solely Ru/RuO$_2$ NPs. The Ru/RuO$_2$ NPs or NP mixtures were studied in hydrogenation of nitrobenzene to aniline. This reaction is frequently used as a standard test for the catalyst activity[22, 23] but also has commercial importance in the aniline production for the polyurethane industry.[24]

Hydrogenation of nitrobenzene has been catalyzed by Au NPs,[25, 26] Pd NPs,[27, 28] Pt NPs,[29] Ru NPs,[28, 30, 31] etc. Although Pd was shown to be the most active catalyst in this reaction,[28] the interest in Ru is growing fast owing to the Ru price being about 9% of the price of Pd.[31] Thus, the design of efficient catalysts based on Ru NPs and including iron oxide NPs allowing magnetic separation, holds great promise for nitrobenzene hydrogenation. In this paper we demonstrate that the solvent type, reaction temperature, and the size and composition of initial iron oxide NPs are the control mechanisms for the reaction outcome including the degree of NP aggregation and the catalytic properties. To assess structure-property relationships, the catalysts were

characterized by transmission electron microscopy (TEM), X-ray powder diffraction (XRD), x-ray photoelectron spectroscopy (XPS), and energy dispersive x-ray spectroscopy (EDS).

Experimental

Materials

$FeCl_3 \cdot 6H_2O$ (98%), octadecane (99%), eicosane (99%), docosane (99%), dioctyl ether (99%), diphenyl ether (≥98%), 1,2-hexadecane diol (90%), oleylamine (OAm, 70%), oleic acid (OA, 90%), $Ru(acac)_3$ (97%), nitrobenzene (NB, 99%), and aniline (99%) were purchased from Sigma-Aldrich and used as received. Hexanes (85%), ethanol (95%), and acetone (99.78%) were purchased from EMD Chemicals and used as received. Chloroform (Mallinckrodt, 100%) was also used without purification.

Synthetic procedures

IRON OXIDE NANOPARTICLE SYNTHESIS

Iron oleate was synthesized according to a published procedure.[32] Iron oxide NPs were prepared via the thermal decomposition of iron oleate in octadecane, eicosane, or docosane as solvents, which were chosen to control the reaction temperature and achieve the desired NP size.[33, 34] The resultant NPs were stored in the solid reaction solution and refrigerated until needed. Oxidation of as-synthesized NPs was carried out according to a procedure described elsewhere.[21, 34] Figure S1 (the Electronic Supplementary Information, ESI) shows a typical NP sample before and after oxidation revealing that oxidation of the iron oxide NPs has nearly no influence on their size and morphology.

SYNTHESIS OF RU/IRON OXIDE NPS

In a typical procedure, chloroform was evaporated in vacuum from a solution containing 15 mg of iron oxide NPs. Then the NPs were dissolved in 7 mL of dioctyl ether and sonicated for 20 min. A three-neck round bottom flask was charged with 0.05 g of 1,2-hexadecane diol, 10 µL of OAm, 10 µL of OA (both OAm and OA were used as surfactants) and the NP solution. The flask was equipped with a reflux condenser, temperature probe, argon inlet, and a stir bar. Argon was bubbled into the solution via a needle for 15 minutes. The solution was then heated at 10 °C/min to 285 °C. Once the solution temperature reached 285 °C, a suspension of 0.025g of $Ru(acac)_3$ in 0.25mL dioctyl ether was injected into the reaction solution, which was kept at 285 °C for 45 minutes while stirring. The solution was then cooled and transferred to a vial. The sample was stored in a refrigerator. The yields of the reaction products are shown in Table 1.

Characterization

Electron-transparent NP specimens for TEM were prepared by placing a drop of a diluted solution onto a carbon-coated Cu grid. Images were acquired at an accelerating voltage of 80 kV on a JEOL JEM1010 transmission electron microscope. Images were analyzed with the National Institute of Health developed image-processing package ImageJ to estimate NP diameters. Between 200 and 300 NPs were used for this analysis. High resolution TEM (HRTEM) images and energy dispersive X-ray spectra (EDS) were acquired at accelerating voltage 300 kV on a JEOL 3200FS transmission electron microscope equipped with an Oxford Instruments INCA EDS system. The same TEM grids were used for all analyses.

X-ray powder diffraction (XRD) patterns were collected on an Empyrean from PANalytical. X-rays were generated from a copper target with a scattering wavelength of 1.54 Å. The step-size of the experiment was 0.02.

XPS experiments were performed using PHI *Versa Probe II* instrument equipped with a monochromatic Al K(alpha) source. The X-ray power of 25 W at 15 kV was used for a 100 micron beam size. The instrument work function was calibrated to give a binding energy (BE) of 84.0 eV for the Au $4f_{7/2}$ line for metallic gold, and the spectrometer dispersion was adjusted to give BEs of 284.8 eV, 932.7 eV and of 368.3 eV for the C 1s line of adventitious (aliphatic) carbon present on the non-sputtered samples, Cu $2p_{3/2}$ and Ag $3d_{5/2}$ photoemission lines, respectively. The PHI double charge compensation system was used on all samples. The ultimate *Versa Probe II* instrumental resolution was determined to be better than 0.125 eV using the Fermi edge of the valence band for metallic silver. XPS spectra with an energy step of 0.1 eV were recorded using software *SmartSoft–XPS* v2.0 and processed using PHI *MultiPack* v9.0 and/or CasaXPS v.2.3.14 at the pass energies of 46.95 eV, 23.5 eV, and 11.75 eV for Fe 2p and Ru 3p, both C 1s and Ru 3d, and O 1s regions, respectively. Peaks were fitted using GL line shapes and/or an asymmetric line shape A(0.2,0.8,0) GL(10), i.e., a combination of Gaussians and Lorentzians with 10-50% of Lorentzian content. A Shirley background was used for curve-fitting. The samples were prepared by drop casting of the NPs solution in chloroform on a native surface of a Si wafer.

X-ray fluorescence (XRF) measurements to determine the Ru content were performed with a Zeiss Jena VRA-30 spectrometer (Mo anode, LiF crystal analyzer and SZ detector). Analyses were based on the Co K_α line and a series of standards prepared by mixing 1 g of polystyrene with 10–20 mg of standard compounds. The time of data acquisition was constant at 10 sec.

Catalysis Science & Technology

ARTICLE

Table 1. Reaction conditions for formation of Ru/iron oxide containing nanoparticles

Sample notation	Iron oxide NP type	Iron oxide NP size, nm	Standard deviation, nm	OA (μL)	OAm (μL)	Solvent	Reaction temp. (°C)	Yield, %[b]	Ru NP size, nm	Standard deviation, nm
Ru-1	Fe_3O_4/γ-Fe_2O_3	8.1	0.7	10	10	dioctyl ether	285	61.8	3.2	0.6
Ru-2	Fe_3O_4/γ-Fe_2O_3	8.1	0.7	5	5	"	285	73.3	2.9	0.4
Ru-3	Fe_3O_4/γ-Fe_2O_3	8.1	0.7	3	3	"	285	65.4	3.0	0.5
Ru-4	Fe_3O_4/γ-Fe_2O_3	8.1	0.7	0	0	"	285	53.3	2.2	0.3
Ru-5	Fe_3O_4/γ-Fe_2O_3	11.0	1.3	10	10	"	285	74.1	2.5	0.6
Ru-6	Fe_3O_4/γ-Fe_2O_3	11.0	1.3	10	10	diphenyl ether	250	61.8	3.1	0.3
Ru-7	Fe_3O_4/γ-Fe_2O_3	11.0	1.3	10	10	"	200	64.5	3.9	0.3
Ru-8	Fe_3O_4/γ-Fe_2O_3	11.0	1.3	10	10	dioctyl ether	200	48.6	3.4	0.7
Ru-9	Fe_3O_4/γ-Fe_2O_3	22.3	1.1	10	10	"	250	81.5	3.3	0.5
Ru-10	Fe_3O_4/γ-Fe_2O_3	22.3	1.1	10	10	"	200	78.2	3.2	0.4
Ru-11	Fe_3O_4/γ-Fe_2O_3	22.6	1.5	10	10	dioctyl ether	285	65.1	2.1	0.4
Ru-12	Fe_3O_4/γ-Fe_2O_3	22.6	1.5	10	10	"	250	65.9	2.7	0.7
Ru-13	FeO-Fe_3O_4	22.6	1.5	15	15	"	285	74.1	3.3	0.5
Ru-14	FeO-Fe_3O_4	22.7	1.8	10	10	diphenyl ether	250	72.3	2.7	0.6
Ru-15	Fe_3O_4/γ-Fe_2O_3	22.6	1.5	10	10	dioctyl ether	285	68.9	2.9	0.3
Ru-16	Fe_3O_4/γ-Fe_2O_3	22.1	2.1	10	10	"	250	77.8	2.9	0.8
Ru-17	Fe_3O_4/γ-Fe_2O_3	27.8	1.9	10	10	"	250	78.8	3.3	0.7
Ru-18	none			10	10	"	285	81.2	3.1	0.8
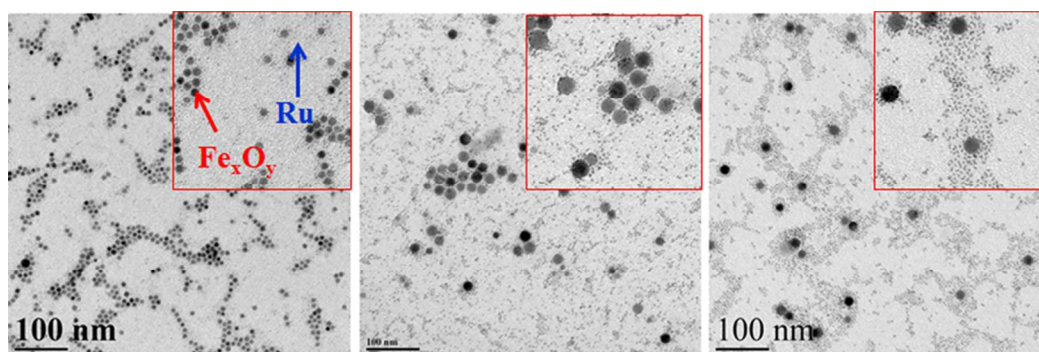
Figure 1. TEM images of Ru-4 (a), Ru-11 (b), and Ru-13 (c). All samples were prepared at 285 °C in dioctyl ether (Table 1). The insets show higher magnification images

Catalytic studies

Catalytic testing was carried out in a 60 mL isothermal stainless-steel batch reactor with a glass insert installed in a shaker and connected to a gasometrical burette (for hydrogen consumption control). The reactor was equipped with two inlets: one for the catalyst, substrate, and solvent, and the other for the hydrogen feed. The total volume of the liquid phase was 30 mL. The reaction was carried out in isopropanol at 30 atm and 150 °C with a stirring rate of 850 shakings per minute. The catalyst was separated after the reaction using a rare earth magnet.

Samples were periodically taken and analyzed via GC-MS (Shimadzu GCMS-QP2010S) equipped with a capillary column HP-1MS (30 m × 0.25 mm i.d., 0.25 μm film thickness). Helium was used as a carrier gas at a pressure of 53.6 kPa and linear velocity of 36.3 cm/s. Analysis conditions: oven temperature 60 °C (isothermal), injector temperature 280 °C, ion source temperature 260 °C, a range from 10 up to 200 m/z. Diphenylamine was used as an internal standard. Calibration curves for nitrobenzene and aniline were used to determine the concentrations of the compounds. Purity of aniline formed was confirmed by mass spectra at high conversions (see Fig. S2, ESI).

Results and Discussion

Influence of the reaction conditions on the NP morphology

IRON OXIDE NPS: STRUCTURE AND PROPERTIES

For the syntheses of Ru-containing catalysts, two types of iron oxide NPs were used as iron source: (1) as-synthesized iron oxide NPs consisting mainly of FeO and a smaller fraction of Fe_3O_4[33] and (2) their oxidized products prepared by heating the reaction solution of the FeO-Fe_3O_4 NPs at 200 °C for 2 h in air.[21, 34] Taking into account the oxidative environment, in our preceding work it was assumed that after oxidation most probably γ-Fe_2O_3 was formed,[34] however the similarity of XRD patterns of magnetite (Fe_3O_4) and maghemite (γ-Fe_2O_3) NPs and line broadening do not allow one to distinguish between these two phases.[35] To clarify the structure of the oxidized iron oxide NPs, we carried out XPS of representative 8.1 nm NPs drop cast on a silicon wafer.

The high resolution Fe 3p XPS spectra taken in several spots on the silicon wafer (Fig. S3, ESI) presented in Figure S4a (ESI) show exceptional uniformity of electronic properties on the micrometer scale. In our preceding paper, it was determined that for the 11 nm oxidized iron oxide NPs, the atomic ratio of Fe^{2+}/Fe^{3+} is 0.18, which matches 54 mol.% of the Fe_3O_4 phase.[36] In general, the values of Fe 2p binding energies (BE) ranging from 710.7 eV to 711.2 eV without satellite structure indicate stoichiometric Fe_3O_4 species.[37, 38] Smaller iron oxide NPs (8.1 nm) in this study exhibit a weak satellite at 718.9 eV BE in the Fe $3p_{3/2}$ region characteristic of Fe^{3+} ions (Fig. S4a, ESI), thus the sample consists largely of Fe^{3+} ions with a minor fraction of the Fe^{2+} ions (see Table S1, ESI). The presence of satellites, however, hinders accurate deconvolution of the XPS spectra from the Fe 2p region (see discussion in ESI). Thus, for assessment of the Fe^{2+}/Fe^{3+} ratio in the 8.1 nm iron oxide NPs, we used the Fe 3p XPS region (Fig. S4b, ESI). The deconvolution of the XPS spectrum shows an average value of 0.15 for the Fe^{2+}/Fe^{3+} ratio in the 8.1 nm NPs (Table S1, ESI), which matches 45 mol.% of the Fe_3O_4 phase.

To study the influence of the iron oxide NP size on the Ru NP formation, two major sizes of initial iron oxide NPs were explored: ~8-11 nm and ~22-23 nm. For smaller iron oxide NP diameters (8-11 nm), only oxidized NPs were employed because for the FeO-Fe_3O_4 NPs, the magnetic separation was too slow. In the case of larger NPs (22-23 nm), both as-prepared (FeO-Fe_3O_4) and oxidized Fe_3O_4/γ-Fe_2O_3 NPs were used because their magnetic separation was sufficiently prompt. Moreover, magnetic measurements showed that the Fe_3O_4/γ-Fe_2O_3 NPs of 22.1 nm diameter are ferrimagnetic at room temperature, while a non-oxidized analog is superparamagnetic (Fig. S5, ESI).

SURFACTANT AMOUNT

Syntheses of Ru-containing NPs were carried out in boiling dioctyl ether (~285 °C), which is a good solvent for iron oxide NPs coated by oleic acid (Table 1). Similar to the syntheses of PtFe NPs,[21] the surfactant loading was decreased to cause destabilization of initial iron oxide NPs and to obtain solely RuFe NPs. However, unlike the PtFe NP case, the decrease of the surfactant loading down to zero surfactant added (Table 1), results in the same outcome: The sample contains a mixture of larger particles whose sizes are consistent with the sizes of the initial iron oxide NPs and smaller, presumably RuFe or Ru NPs (Fig. 1). The change of the iron oxide NP size or composition does not change the reaction outcome (Fig. 1), thus indicating that Ru NPs are well stabilized with very low amounts of

surfactants presumably coming off the surface of the initial iron oxide NPs.

REACTION SOLVENT AND 250 °C REACTION TEMPERATURE

To evaluate the influence of the solvent nature on the reaction product, the reaction was also carried out in diphenyl ether which, compared to dioctyl ether, has lower affinity towards NPs coated with OA or OAm (for Ru-containing NPs) but higher affinity towards Ru(acac)$_3$ (immediate dissolution at room temperature). At the same time, the reaction solution in diphenyl ether has a lower boiling point: 250 °C. To make a valid comparison, the reactions at 250 °C were carried out in both diphenyl and dioctyl ethers for smaller and larger iron oxide NPs (Table 1). The reaction in diphenyl ether at 250 °C with 11.0 nm Fe$_3$O$_4$/γ-Fe$_2$O$_3$ NPs (Ru-6, Table 1 and Fig. S6c, ESI) produced a mixture of two types of NPs similar to those shown in Figure 1. For larger (22.7 nm) iron oxide NPs of the same composition used in dioctyl ether at 250 °C (Ru-12, Table 1 and Fig. S6a, ESI), some aggregation took place. A similar reaction product was obtained for 22.7 nm FeO-Fe$_3$O$_4$ NPs in diphenyl ether at 250 °C (Ru-14, Table 1 and Fig. S6b, ESI). To prove that aggregation existed in the reaction product and did not occur on the TEM grid, we carried out DLS measurements. The DLS intensity distributions vs. hydrodynamic diameters (D_h) of Ru-12 and Ru-14 are shown in Figure 2. The peaks with maxima at 35-45 nm are due to individual iron oxide NPs surrounded with Ru NPs or due to a few NP dimers. The peaks at 99 nm for Ru-14 and 191 nm for Ru-12 are due to aggregates. In contrast, Ru-13 obtained in dioctyl ether at 285 °C contains only a minor fraction of aggregates (Fig. 2) while the major fraction is the 25 nm NPs, suggesting a good NP dispersion.
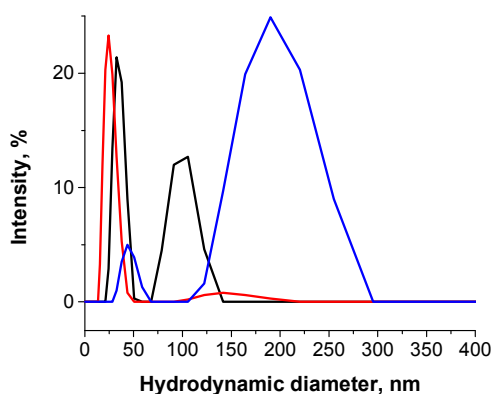
Figure 2. DLS intensity distributions vs. hydrodynamic diameter for Ru-12 (blue), Ru-14 (black), and Ru-13 (red).

To assess the composition of both kinds of NPs present in the resultant sample, the Ru-14 sample was evaluated using HRTEM and EDS. Figure 3 shows the HRTEM image of large crystalline NPs surrounded by much smaller NPs. The distance between lattice fringes in larger particles is 2.48 Å, which corresponds to the separation between the (311) planes in

Fe$_3$O$_4$.[37, 38] The lattice fringe distance in small NPs is 2.1 Å corresponding to the separation between (101) planes of bulk ruthenium.[39]
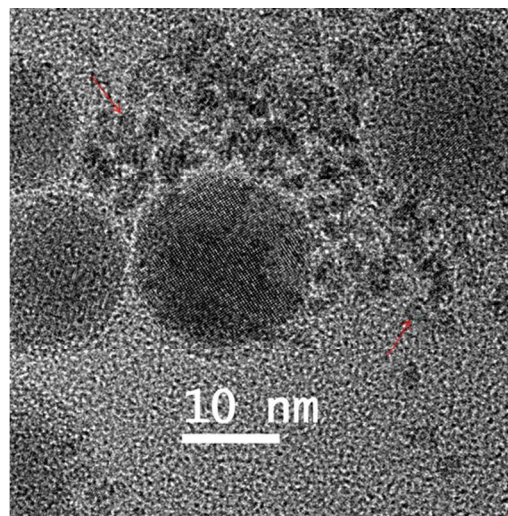
Figure 3. HRTEM image of the Ru-14 sample. Red arrows show small, presumably Ru NPs.

The EDS maps of the larger NPs (Fig. S7, ESI) exhibit mainly the presence of iron, while Ru is hardly detectable. Alternatively, the EDS maps of the smaller NPs (Fig. 4) show Ru but no Fe: the Fe map (Fig. 4c) exhibits mainly noise. Thus, the small particles consist of only Ru.
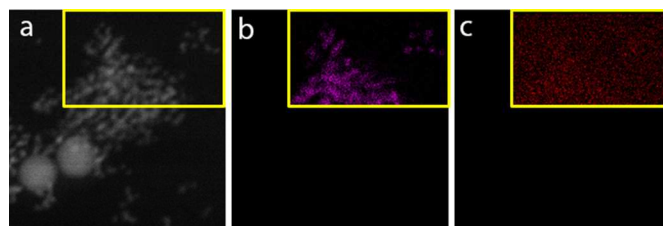
Figure 4. Dark-field STEM image (a) and Ru (b) and Fe (c) maps obtained by STEM EDS of Ru-14. The yellow square shows a part of the dark-field image mapped by EDS.

The XRD pattern of the same sample (Fig. S8, ESI) shows two sets of the reflections indicative of two phases. Sharp signals at 2θ = 30.3, 35.6, 43.3, 54.0, 57.2, and 62.9° correspond to the (220), (311), (400), (422), (511), and (440) crystallographic planes of a spinel phase (magnetite or maghemite).[40, 41] Considering that the initial iron oxide NPs in this case were FeO-Fe$_3$O$_4$, additional oxidation may occur with OA and/or acetylacetone during Ru NP formation. The broad signal at 2θ of about 43° is due to Ru(0), although line broadening does not allow us to distinguish between the fcc and hcp Ru phases.[42, 43] No signals associated with RuO$_2$ were detected.[44]

The survey XPS spectrum of Ru-14 presented in Figure S9 (ESI) shows Ru, Fe, C, O, and Si. The last comes from the silicon wafer support. The high resolution Fe 3p XPS spectra of Ru-14 taken in several spots of the sample surface (Fig. S10, ESI) are presented in Figure S11 (ESI). The deconvolution of

the representative spectrum (Fig. S12, Table S2, ESI) demonstrates the presence of both Fe^{2+} and Fe^{3+} species, with an average Fe^{2+}/Fe^{3+} atomic ratio of 0.47 which is close to the stoichiometric ratio in Fe_3O_4 ($Fe^{2+}/Fe^{3+}=0.5$) (Table S2, ESI). This finding along with disappearance of the satellite structure at 719 eV BE in the Fe 2p region (Fig. S13a, ESI) proves once more the transformation of $FeO-Fe_3O_4$ into magnetite.

The high resolution XPS spectrum of Ru-14 in the Ru 4p and 3p regions is presented in Figure 5. According to the deconvolution of this region, the components at 461.31 eV and 463.16 eV BE are assigned to the Ru^0 and Ru^{4+} species, respectively. The measured BE values are consistent with those reported for Ru nanoparticles.[45] The deconvolution shows an Ru^{4+}/Ru^0 average ratio of 0.57 (Table S3, ESI). Formation of a RuO_2 layer on Ru(0) NPs is well-established when NPs are exposed to air.[46] The absence of the RuO_2 reflections in the XRD pattern of this sample indicates that the RuO_2 is either amorphous or the crystallites are too small. It is noteworthy that the Ru-14 sample demonstrates remarkable stability upon argon sputtering. The high resolution Fe 2p, Ru 3d, and valence band spectra show no changes in BE (Fig. S13, ESI) after a 1 min 1 kV cycle of argon sputtering.
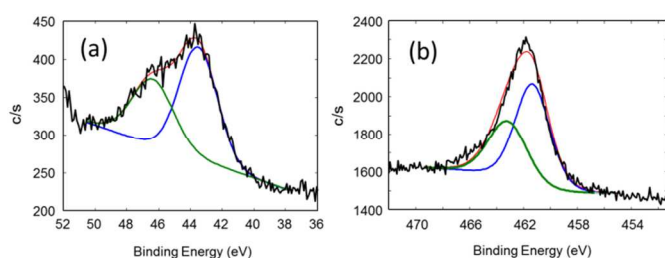
Figure 5. High resolution Ru 4p (a) and 3p (b) XPS of Ru-14 with deconvolution. See Table S3 (ESI) for fitting parameters. Black line represents experimental data, blue and green lines show the Ru^0 and Ru^{4+} components, respectively, while the red line represents simulated spectra.

DIPHENYL ETHER AND 200 °C REACTION TEMPERATURE

A further decrease of the reaction temperature to 200 °C in diphenyl ether leads to two different outcomes depending on the $Fe_3O_4/\gamma-Fe_2O_3$ NP size. For the 11 nm $Fe_3O_4/\gamma-Fe_2O_3$ NPs, significant aggregation of iron oxide and small Ru NPs takes place resulting in a sample (Ru-7, Fig. 6a), whose magnetic separation occurs within a few minutes. The DLS trace (Fig. S14, ESI) of Ru-7 (Table 1, Fig. 6a) shows only aggregates. At 200 °C aggregation occurs even in dioctyl ether (Ru-8, Table 1 and Fig. S14, ESI), which has higher affinity for these NPs.
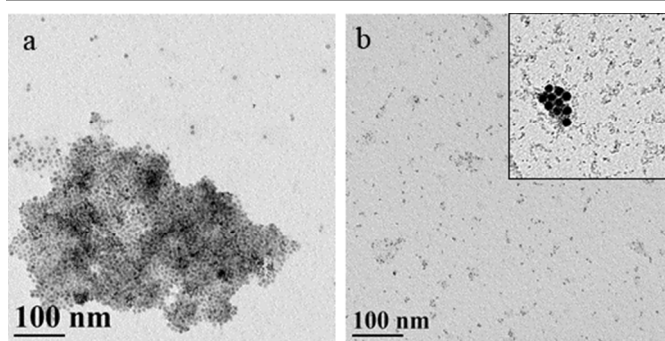
Figure 6. TEM images of Ru-7 (a) and Ru-10(b). Inset in (b) shows an image with a few initial iron oxide NPs.

In the case of 22.3 nm $Fe_3O_4/\gamma-Fe_2O_3$ NPs, the sample contains nearly exclusively small NPs (Ru-10, Fig. 6b) with only a few initial iron oxide NPs (inset in Fig. 6b). When the reaction was carried out with the largest $Fe_3O_4/\gamma-Fe_2O_3$ NPs used in this work (27.8 nm, Ru-17), solely small NPs were formed while all the $Fe_3O_4/\gamma-Fe_2O_3$ NPs were removed (Fig. S15a, ESI), indicating that the larger the iron oxide NPs, the higher the tendency to aggregation. The XRD pattern of this sample (Fig. S15b, ESI) shows only reflections typical of Ru metal.[42] The survey XPS spectrum of Ru-17 presented in Figure S16 (ESI) exhibits Ru, C, O, and Si. No Fe signals were detected. The deconvolution of the XPS spectrum of Ru-17 in the Ru 3p and Ru 4p regions (Fig. S17) indicates an average Ru^{4+}/Ru^0 ratio of 0.58 (Table S4, ESI), which is consistent with that of Ru-14. Again, the Ru-17 NPs demonstrate excellent stability upon argon sputtering (Figs. S18-20, ESI).

It is worth noting that although reference Ru NPs prepared without iron oxide (Ru-18, Table 1 and Fig. S15c, ESI) have a similar NP size as those in Ru-17, they exhibit a tendency to aggregation, while the Ru-17 NP are perfectly dispersed.

Mechanism of aggregation or destabilization of $Fe_3O_4/\gamma-Fe_2O_3$ NPs

To understand different reaction outcomes described above, we selected two key reaction procedures, taking samples of the reaction solution 5, 15, and 25 minutes after the injection of the $Ru(acac)_3$ solution. Figure S21 (ESI) presents TEM images of such samples taken from the reaction solution of Ru-7 prepared at 200 °C in diphenyl ether in the presence of 11.0 nm $Fe_3O_4/\gamma-Fe_2O_3$ NPs (Fig. 5a). In the sample taken after 5 min no Ru NPs are formed (Fig. S21a, ESI), while iron oxide NPs already begin to aggregate. After 15 min the aggregation becomes more pronounced and a few small particles are visible in the vicinity of the aggregate (inset to Fig. S21b, ESI). The TEM image of the sample taken after 25 min shows an aggregate of iron oxide NPs surrounded by numerous small (Ru) NPs (Fig. S21c, ESI). The question arises, however, what is the cause of such aggregation especially considering that the iron oxide NPs used in the reaction were well stabilized by surfactants?
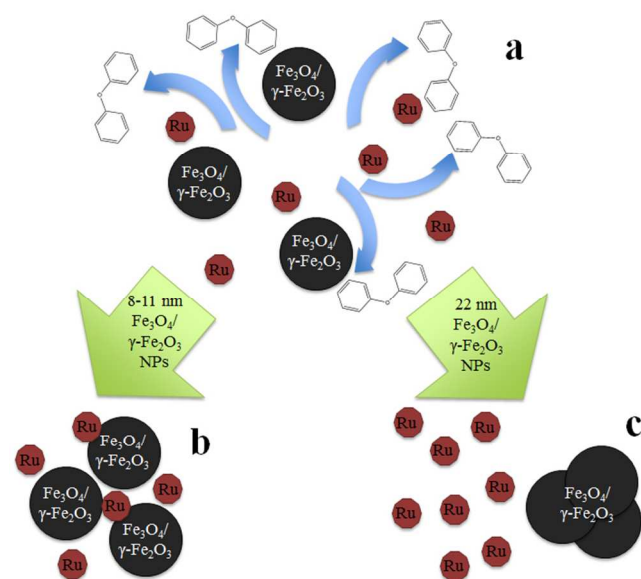
Scheme 1. (a) Segregation of Pd and iron oxide NPs from solvent due to polarization forces. (b) Aggregation Ru and small (8-11 nm) Fe_3O_4/γ-Fe_2O_3 NPs together. (c) Destabilization and removal of large (22-28 nm) Fe_3O_4/γ-Fe_2O_3 NPs.

The NP interactions in solution are governed by multiple nanoscale forces including van der Waals, electrostatic, magnetic, surface, and depletion effects.[47, 48] Depletion forces are considered the most influential in the NP self-assembly in the presence of large molecules[49] or even excess of regular surfactants.[48] However, in our case, the variations in the surfactant amounts did not change the reaction outcome. In this case, the polarization forces might play a considerable role.[49, 50] Indeed, the Ru metal dielectric constant is 82 ± 10.[51] The dielectric constant of ferric oxide is 13.1,[31] while for diphenyl ether it is only 3.9.[31] The data for dioctyl ether are not published, but dioctyl phthalate has a dielectric constant of 5.1.[31] Thus, polarization force could be a trigger causing segregation of both types of particles from the solvent, leading to NP aggregation, which is pronounced at lower reaction temperatures and in the less favourable (for NP dissolution) solvent (diphenyl ether) (Scheme 1). However, when aggregation of iron oxide NPs initiates, their collective magnetic properties change due to a change in dipole–dipole interactions and they may begin exhibiting ferrimagnetic behaviour, despite the individual NPs being superparamagnetic.[47] This may result in magnetic attraction towards surrounding iron oxide NPs, causing further aggregation (Scheme 1b) and even destabilization of large iron oxide NPs (Scheme 1c). Both polarization and magnetic forces can be offset by the active Brownian motion at higher temperatures and in better solvents (dioctyl ether).

A close look at the majority of TEM images reveals no heterogeneous nucleation of Ru NPs: They are not attached to the iron oxide NP surface. These Ru NPs form a cloud around iron oxide NP aggregates and this cloud moves together with the aggregates upon magnetic separation due to polarization forces as the Ru NPs are not superparamagnetic. At the same

time, multiple magnetic separations of such a sample show no further loss of Ru NPs after some initial removal (see below).

When the Fe_3O_4/γ-Fe_2O_3 NPs are large (22-23 or 27.8 nm), their aggregation and precipitation at both 200 and 250 °C takes place. Indeed, already 5 min after the injection of the $Ru(acac)_3$ solution, they are practically absent in the sample (Fig. S22, ESI). The majority of the sample consists of very small Ru NPs, indicating that they are not aggregated together with the iron oxide NPs. This may occur due to fast aggregation of iron oxide NPs before formation of Ru NPs, mainly due to a combination of polarization effects and magnetic interactions. The inset in Figure S22d (ESI) shows the iron oxide NPs tend to aggregate after heating to 250 °C in diphenyl ether even before addition of $Ru(acac)_3$.

Catalytic behaviour

As is demonstrated above, the nature of the solvent, reaction temperature and the size and composition of initial iron oxide NPs are the control mechanisms for designing novel Ru-based materials. The question arises, however, whether this design can allow control over catalytic performance? To assess the possibility of such a control, we studied the catalytic behaviour of representative Ru-containing samples in hydrogenation of nitrobenzene to aniline (Scheme 2).
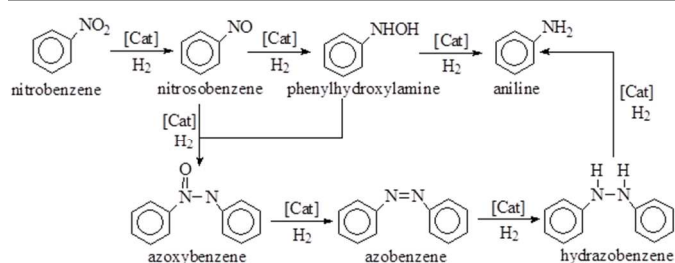
Scheme 2. Hydrogenation of nitrobenzene to aniline. The scheme shows several probable pathways to aniline and numerous possible side products.

The samples chosen differ by the type of the initial iron oxide NPs and by the morphology of the resultant catalysts. These catalysts were compared with Ru/SiO_2 and Pd/SiO_2 whose catalytic properties in nitrobenzene hydrogenation were reported elsewhere.[28] In ref. 28, the TOF values for these catalysts were reported. However, considering that the metal content was estimated only by loading, actually the authors presented reaction rates (not TOF), allowing us direct comparison with the results of this work. In addition, for comparison, we also used the partially aggregated Ru NPs prepared in the conditions of the present paper but without iron oxide NPs (Ru-18, Tables 1 and 2) and the 22.7 nm FeO-Fe_3O_4 NPs used for the Ru-14 synthesis (Fig. S25, ESI). To determine optimal reaction conditions, a series of experiments was carried out for Ru-5 at the overall pressure P=30 bar in the temperature range of 120-180 °C upon variation of the catalyst concentrations in the range of 2-6 g/L and nitrobenzene concentrations in the range of 0.06-0.4 μmol/L (Fig. S23, ESI). The optimal conditions for Ru-5, indicated in the footnote of Table 2, were used for testing of all other catalysts. It is worth

noting that the FeO-Fe$_3$O$_4$ NPs demonstrated poor performance in the nitrobenzene hydrogenation (Fig. S24, ESI, and Table 2). For Ru-18, i.e., the ruthenium NPs prepared in the absence of iron oxide NPs, hydrogenation of nitrobenzene occurred very slowly with extremely low conversion and selectivity (Table 2). For the Ru NPs formed in the conditions of destabilization and precipitation of iron oxide NPs (Ru-16, Tables 1 and 2), the reaction rate as well as the aniline yield and conversion are higher. Considering that the Ru NP sizes in these two samples are comparable (3.1 nm and 2.9), the lower activity and selectivity of the former sample are due to considerable aggregation of the Ru NPs significantly decreasing the amount of available active sites.

The coexistence of the Ru and iron oxide NPs in the catalyst (Ru-5 and Ru-11) leads to a significantly higher aniline yield and higher reaction rates. This is consistent with observations by us[21] and others[52] regarding the influence of iron oxide NPs on catalytic hydrogenation. Although Ru NPs are not deposited on the iron oxide NPs, their close proximity can result in collisions, leading to interactions and electron transfer from the iron oxide NP surface to the Ru surface, facilitating hydrogenation due to partial reduction.[52] On the other hand, Ru-5 and Ru-11 were synthesized in dioctyl ether at 285 °C, i.e., in the conditions where the minimum aggregation of iron oxide and Ru NPs took place, which should decrease the iron oxide influence. Alternatively, for Ru-7, whose aggregation is shown in Figure 6a, a significant increase of aniline yield and conversion are observed accompanied by a noticeable increase of the reaction rate. This is due to direct positioning of Ru NPs on iron oxide NPs within the aggregate. Magnetic separation of Ru-7 followed by several repeated uses shows nearly no changes in the catalyst performance, indicating high stability of this catalyst and complete catalyst recovery.

In the case of Ru-12, whose synthesis was carried out in dioctyl ether at 250 °C, more aggregation takes place than at 285 °C which should allow stronger influence on the catalysis by Ru NPs. Indeed, this leads to the higher conversion and reaction rate. It is worth noting that when Ru-12 was magnetically separated before use with some loss of Ru NPs (Table 2) but with improved recovery, this led to the remarkably high reaction rate. This catalyst was also used several times in the catalytic reaction after magnetic separation and demonstrated excellent stability of the catalytic performance (Table 2).

The analogous sample but prepared with initial FeO/Fe$_3$O$_4$ (Ru-14) shows the 99% aniline yield, 100% conversion and the reaction rate comparable to Pd/SiO$_2$[28], thus revealing that although some aggregation of the Ru and iron oxide NPs is necessary for improved catalytic performance, the nature of iron oxide NPs also plays important role. As was discussed above, Ru-14 includes magnetite NPs, while in Ru-12, the iron oxide NP surface contains maghemite. Thus, the above data indicate that the presence of the Fe^{2+} ions in the iron oxide NPs is crucial for controlling the selectivity of the nitrobenzene hydrogenation. The aniline yield and conversion for both Ru-14 and Ru-12 significantly surpass those achieved with Ru/SiO$_2$

and even Pd/SiO$_2$ reported elsewhere[28] at similar or much higher reaction rates (Table 2).

Table 2. Catalytic properties in hydrogenation of nitrobenzene.[a]

Sample notation	Ru content wt.%	Ru NP size nm	Max. aniline yield, %	Max. conver- sion, %	Time, min	Reaction rate, NB mol converted/ mol Ru ×s
22.7 nm FeO-Fe$_3$O$_4$ NPs	-	-	2	2	90	$0.018×10^{-3}$
Ru-18	38.7	3.1	27	28	140	0.04
Ru-16	58.7	2.9	55	55	70	0.1
Ru-5	20.2	2.5	91	92	180	0.2
Ru-11	3.7	2.1	82	82	170	1.0
Ru-7	7.8	2.5	93	93	50	1.8
Ru-7, 2nd use	7.8	2.5	92	94	60	1.7
Ru-7, 5th use	7.8	2.5	92	93	60	1.6
Ru-12	2.6	2.7	91	97	40	6.8
Ru-12$_{ms}$[b]	0.6	2.7	90	98	15	258
Ru-12$_{ms}$, 2nd use	0.6	2.7	90	97	15	249
Ru-12$_{ms}$, 5th use	0.6	2.7	89	98	15	240
Ru-14	9.5	2.7	99	100	40	2.2
Ru/SiO$_2$[28]	5	-	23	9.7	-	0.03
Pd/SiO$_2$[28]	5 (Pd)	-	77	74	-	3.0

[a]Conditions of hydrogenation: temperature 150°C, nitrobenzene concentration 0.06 µmol/L, pressure 30 bar, catalyst concentration 3 g/L;
[b]After magnetic separation of the initial catalyst.

For Ru-14, displaying highest values of the aniline yield, we again assessed the influence of the catalytic reaction conditions (temperature, catalyst, and nitrobenzene concentrations) on the catalyst performance. The data obtained (not shown) demonstrated that optimal conditions are the same as those found for Ru-5. To assess the morphology of the catalyst after the catalytic reaction, we analyzed the Ru-14 catalyst magnetically separated from the reaction mixture. The comparison of the TEM images presented in Figures S25 and S5b (ESI) shows that the Ru-14 catalyst morphology does not change after hydrogenation.

The apparent activation energies calculated for Ru-5, Ru-12, and Ru-14 samples are 28±5 kJ/mol, 33±5 kJ/mol and 45±5 kJ/mol, while the pre-exponential factors are 17,847, 35,849 and 31,294 (Fig. S26, ESI). The highest activity of Ru-12 sample correlates well with the medium activation energy and the highest pre-exponential factor that can be attributed to the highest amount of active sites on Ru NPs.[53-55]

Conclusions

In summary, we developed a new method for preparation of catalysts containing a mixture of Ru and iron oxide NPs. XPS demonstrates the presence of both Ru^0 and Ru^{4+} species with the Ru^{4+}/Ru^0 average ratio of 0.57, indicating the presence of the RuO$_2$ layer on the Ru(0) NPs. The absence of the RuO$_2$

reflections in the XRD pattern of this sample indicates that the RuO_2 is either amorphous or the crystallites are too small.

The presence of iron oxide NPs in these samples allows efficient magnetic recovery and influences the catalytic properties of Ru/RuO_2 NPs. Moreover, this influence is better utilized when there is at least partial aggregation of Ru and iron oxide NPs, which presumably takes place due to polarization forces combined with magnetic forces. To achieve such aggregation, the catalyst syntheses are carried out at a lower reaction temperature (200-250 °C) and in a less favourable for NPs solvent: diphenyl ether. However, for larger iron oxide NPs in these conditions, destabilization and precipitation of iron oxide NPs takes place leaving the catalyst consisting of solely Ru/RuO_2 NPs with rather mediocre catalytic properties. We also demonstrated that the highest catalyst reaction rate is observed with iron oxide NPs containing maghemite, while the highest aniline yield is achieved with magnetite NPs.

Acknowledgements

Notes and references

[a] Indiana University, Department of Chemistry, 800 E. Kirkwood Av., Bloomington, IN 47405, USA.
[b] Indiana University, Department of Biology, 1001 East Third Street, Bloomington, IN 47405, USA.
[c] Tver State Technical University, Department of Biotechnology and Chemistry, 22 A. Nikitina St, 170026, Tver, Russia.
[d] King Abdulaziz University, Faculty of Science, Department of Physics, Jeddah, Saudi Arabia

.
† *To whom correspondence should be addressed: lybronst@indiana.edu

Electronic Supplementary Information (ESI) available: TEM, XPS, hysteresis curves, STEM, EDS, XRD, DLS, kinetics data, and Arrhenius plots. See DOI: 10.1039/b000000x/

1. Lu, A.-H.; Salabas, E. L.; Schueth, F. *Angew. Chim. Int. Ed. and references therein* **2007,** 46, (8), 1222-1244
2. Chang, B.; Tian, Y.; Shi, W.; Liu, J.; Xi, F.; Dong, X. *RSC Advances* **2013,** 3, (43), 20999-21006.
3. Dai, Q.; Wang, J.; Yu, J.; Chen, J.; Chen, J. *Appl. Catal. B: Env.* **2013,** 144, 686-693.
4. Bazgir, A.; Hosseini, G.; Ghahremanzadeh, R. *ACS Comb. Sci.* **2013,** 15, (10), 530-534.
5. Kundu, D.; Chatterjee, T.; Ranu, B. C. *Adv. Synth. Catal.* **2013,** 355, (11-12), 2285-2296.
6. Wang, D.; Astruc, D. *Chem. Rev.* **2014,** 114, (14), 6949-6985.
7. Wang, Z.; Shen, B.; Zou, A.; He, N. *Chem. Eng. J.* **2005,** 113, (1), 27-34.
8. Zhu, Y.; Peng, S. C.; Emi, A.; Su, Z.; Monalisa;; Kemp, R. A. *Adv. Synth. Cat.* **2007,** 349, (11-12), 1917-1922.
9. Polshettiwar, V.; Luque, R.; Fihri, A.; Zhu, H.; Bouhrara, M.; Basset, J.-M. *Chem. Rev.* **2011,** 111, (5), 3036-3075.
10. Rossi, L. M.; Silva, F. P.; Vono, L. L. R.; Kiyohara, P. K.; Duarte, E. L.; Itri, R.; Landers, R.; Machado, G. *Green Chem.* **2007,** 9, (4), 379-385.
11. Saha, A.; Leazer, J.; Varma, R. S. *Green Chem.* **2012,** 14, (1), 67-71.
12. Vaddula, B. R.; Saha, A.; Leazer, J.; Varma, R. S. *Green Chem.* **2012,** 14, (18), 2133-2136.
13. Sun, W.; Li, Q.; Gao, S.; Shang, J. K. *Appl. Catal., B* **2012,** 125, 1-9.
14. Baig, R. B. N.; Varma, R. S. *Chem. Comm.* **2012,** 48, (50), 6220-6222.
15. Gorbanev, Y. Y.; Kegnaes, S.; Riisager, A. *Top. Catal.* **2011,** 54, (16-18), 1318-1324.
16. Polshettiwar, V.; Varma, R. S. *Chem.-Europ.J.* **2009,** 15, (7), 1582-1586.
17. Baruwati, B.; Polshettiwar, V.; Varma, R. S. *Tetrahedron Lett.* 50, (11), 1215-1218.
18. Mizuno, N.; Yamaguchi, K. *Catal. Today* **2008,** 132, (1-4), 18-26.
19. Kotani, M.; Koike, T.; Yamaguchi, K.; Mizuno, N. *Green Chem.* **2006,** 8, (8), 735-741.
20. Basinska, A.; Klimkiewicz, R.; Domka, F. *Appl. Catal. A: Gen.* **2001,** 207, (1,2), 287-294.
21. Gumina, G.; Easterday, R.; Malyutin, A. G.; Budgin, A. M.; Stein, B. D.; Nikoshvili, L. Z.; Matveeva, V. G.; Sulman, E. M.; Morgan, D. G.; Bronstein, L. M. *Nanoscale* **2013,** 5, (7), 2921-2927.
22. Gelder, E. A.; Jackson, S. D.; Lok, C. M. *Catal. Lett.* **2002,** 84, (205-208).
23. Watt, J.; Cheong, S.-S.; Toney, M. F.; Ingham, B.; Cookson, J.; Bishop, P. T.; Tilley, R. D. *ACS Nano* **2010,** 4, (1), 396-402.
24. http://www.avantilipids.com/
25. Torres, C.; Campos, C.; Fierro, J. L. G.; Oportus, M.; Reyes, P. *Catal. Lett* **2013,** 143, (8), 763-771.
26. Kartusch, C.; Makosch, M.; Sa, J.; Hungerbuehler, K.; van Bokhoven, J. A. *ChemCatChem* **2012,** 4, (2), 236-242.
27. Chatterjee, M.; Chatterjee, A.; Kawanami, H.; Ishizaka, T.; Suzuki, T.; Suzuki, A. *Adv. Synth. Cat.* **2012,** 354, (10), S2009/1-S2009/9.
28. Tamura, M.; Kenichi, K.; Satsuma, A.; Shimizu, K. *ACS Catalysis* **2012,** 2, (9), 1904-1909.
29. Fan, G.; Wang, Y.; Wang, C. *RSC Adv.* **2014,** 4, (21), 10997-11002.
30. Chary, K. V. R.; Srikanth, C. S. *Catal. Lett* **2009,** 128, (1-2), 164-170.
31. Ding, Y.; Li, X.; Pan, H.; Wu, P. *Catal. Lett* **2014,** 144, (2), 268-277.
32. Park, J.; An, K.; Hwang, Y.; Park, J.-G.; Noh, H.-J.; Kim, J.-Y.; Park, J.-H.; Hwang, N.-M.; Hyeon, T. *Nature Mater.* **2004,** 3, (12), 891-895.
33. Bronstein, L. M.; Huang, X.; Retrum, J.; Schmucker, A.; Pink, M.; Stein, B. D.; Dragnea, B. *Chem. Mater.* **2007,** 19, (15), 3624-3632.
34. Bronstein, L. M.; Atkinson, J. E.; Malyutin, A. G.; Kidwai, F.; Stein, B. D.; Morgan, D. G.; Perry, J. M.; Karty, J. A. *Langmuir* **2011,** 27, (6), 3044-3050.
35. Hou, Y.; Xu, Z.; Sun, S. *Angew. Chim. Int. Ed.* **2007,** 46, (33), 6329-6332.

36. Easterday, R.; Sanchez-Felix, O.; Stein, B. D.; Morgan, D. G.; Maren, P.; Losovyj, Y.; Bronstein, L. M. *J. Phys. Chem. C* **2014,** 118, (42), 24769-24775.

37. Zhu, Y.; Jiang, F. Y.; Chen, K.; Kang, F.; Tang, Z. K. *J. Alloys Compd.* **2011,** 509, (34), 8549-8553.

38. Shi, W.; Zhu, J.; Sim, D. H.; Tay, Y. Y.; Lu, Z.; Zhang, X.; Sharma, Y.; Srinivasan, M.; Zhang, H.; Hng, H. H.; Yan, Q. *J. Mater. Chem.* **2011,** 21, (10), 3422-3427.

39. Bonnefille, E.; Novio, F.; Gutmann, T.; Poteau, R.; Lecante, P.; Jumas, J.-C.; Philippot, K.; Chaudret, B. *Nanoscale* 6, (16), 9806-9816.

40. Cornell, R. M.; Schwertmann, U., *The Iron Oxides*. VCH: New York, 1996.

41. Guo, J.; Gu, H.; Wei, H.; Zhang, Q.; Haldolaarachchige, N.; Li, Y. Y.; P.;, D.; Wei, S.; Guo, Z. *J. Phys. Chem. C* **2013,** 117, (19), 10191-10202.

42. Kusada, K.; Kobayashi, H.; Yamamoto, T.; Matsumura, S.; Sumi, N.; Sato, K.; Nagaoka, K.; Kubota, Y.; Kitagawa, H. *J. Am. Chem. Soc.* **2013,** 135, (15), 5493-5496.

43. Yang, J.; Lee, J. Y.; Deivaraj, T. C.; Too, H.-P. *J. Coll. & Interface Sci.* **2004,** 271, (2), 308-312.

44. Lin, Y.; Zhao, N.; Nie, W.; Ji, X. *J. Phys. Chem. C* **2008,** 112, (42), 16219-16224.

45. Chakroune, N.; Viau, G.; Ammar, S.; Poul, L.; Veautier, D.; Chehimi, M. M.; Mangeney, C.; Villain, F.; Fiévet, F. *Langmuir* **2005,** 21, (15), 6788-6796.

46. Novio, F.; Monahan, D.; Coppel, Y.; Antorrena, G.; Lecante, P.; Philippot, K.; Chaudret, B. *Chem. Eur. J.* **2014,** 20, (5), 1287-1297.

47. Bishop, K. J. M.; Wilmer, C. E.; Soh, S.; Grzybowski, B. A. *Small* **2009,** 5, (14), 1600-1630.

48. Ye, X.; Millan, J. A.; Engel, M.; Chen, J.; Diroll, B. T.; Glotzer, S. C.; Murray, C. B. *Nano Lett.* **2013,** 13, (10), 4980-4988.

49. Israelachvili, J. N., *Intermolecular and Surface Forces* Third ed.; Academic Press: 2011; p 709.

50. Gomila, G.; Esteban-Ferrer, D.; Fumagalli, L. *Nanotechnology* **2013,** 24, (50), 505713/1-505713/8.

51. Choi, W. S.; Seo, S. S. A.; Kim, K. W.; Noh, T. W.; Kim, M. Y.; Shin, S. *Phys. Rev. B* **2006,** 74, (20), 205117/1-205117/8.

52. Milone, C.; Crisafulli, C.; Ingoglia, R.; Schipilliti, L.; Galvagno, S. *Catal. Today* **2007,** 122, (304), 341-351.

53. Hansen, N.; Heyden, A.; Bell, A. T.; Keil, F. J. *J. Catal.* **2007,** 248, (2), 213-225.

54. Hoshi, N.; Asaumi, Y.; Nakamura, M.; Mikita, K.; Kajiwara, R. *J. Phys. Chem. C* **2009,** 113, (39), 16843-16846.

55. Marban, G.; del Rio, L. *Kinet. Catal.* **2013,** 54, (4), 463-468.

Catalysis Science & Technology   RSC**Publishing**

TOC graphic